

Optical Detection and Spatial Modulation of Mid-Infrared Surface Plasmon Polaritons in a Highly Doped Semiconductor

Davide Maria Di Paola, Anton V. Velichko, Mario Bomers, Nilanthy Balakrishnan, Oleg Makarovskiy, Mario Capizzi, Laurent Cerutti, Alexei N. Baranov, Manoj Kesaria, Anthony Krier, Thierry Taliercio, and Amalia Patanè**

Highly doped semiconductors (HDSCs) are promising candidates for plasmonic applications in the mid-infrared (MIR) spectral range. This work examines a recent addition to the HDSC family, the dilute nitride alloy In(AsN). Postgrowth hydrogenation of In(AsN) creates a highly conducting channel near the surface and a surface plasmon polariton detected by attenuated total reflection techniques. The suppression of plasmonic effects following a photoannealing of the semiconductor is attributed to the dissociation of the N–H bond. This offers new routes for direct patterning of MIR plasmonic structures by laser writing.

1. Introduction

Plasmonics generally relies on metals due to the high density of free electrons. However, metals also suffer from substantial losses due to interband transitions, grain-boundary

scattering in thin films, surface roughness, etc.; chemical instability in air and low compatibility with silicon technology represent further limitations to the exploitation of metals;^[1] also, given their high carrier densities (10^{22} – 10^{23} cm⁻³), metals usually have plasma frequencies, ω_p , in the visible–UV spectral ranges. On the other hand, highly doped semiconductors (HDSCs) present several appealing features:^[2,3] first, the lower carrier densities (10^{16} – 10^{20} cm⁻³) enable plasma frequencies in the mid-infrared (MIR) spectral range, of relevance for technologically important

applications, including gas detection and biosensing;^[4,5] second, the carrier density and the plasmonic resonance can be tuned either by doping or geometrical patterning of semiconductors,^[6] thus enabling routes to cost-effective and compact all-semiconductor plasmonic structures.^[7,8]


Achieving a high doping in a semiconductor can be limited by the solid solubility of the dopants^[9,10] and/or by doping compensation effects.^[11,12] In addition, a high density of dopants can degrade the crystal quality and induce internal losses. Thus, finding low-loss semiconductor materials for plasmonics presents challenges of fundamental and technological interest.^[13] To date, a number of HDSCs have been successfully tested, including transparent conducting oxides, such as aluminum and gallium zinc oxide,^[14] indium tin oxide,^[15] and dysprosium cadmium oxide.^[16] These materials have plasmonic resonances in the near-infrared^[14,15] and MIR spectral range.^[16] Compounds such as SiC,^[17] (InGa)As,^[18] and In(AsSb)^[6,8,19] have also shown good response in the MIR.^[20] The III–V semiconductor InAs features as a relatively recent addition to this group: it can sustain high doping concentrations^[10,21] with plasmonic resonances over a broad MIR range.^[22] Furthermore, the incorporation of small quantities of nitrogen ($N < 3\%$) into the group-V sublattice of InAs to form the dilute nitride alloy In(AsN) enables the engineering of fundamental band properties and the behavior of dopants.^[23,24] For example, the incorporation of nitrogen in InAs reduces the band gap energy of the material, while that of hydrogen in In(AsN) increases the electron density by two orders of magnitude, up to 10^{19} cm⁻³.^[25] This enhancement, not observed in InAs or reported for other dilute nitride alloys, is due to the N-atoms, which act as H traps to form N–H donor complexes

D. M. Di Paola, Dr. A. V. Velichko, Dr. N. Balakrishnan, Dr. O. Makarovskiy, Prof. A. Patanè
School of Physics and Astronomy
The University of Nottingham
Nottingham NG7 2RD, UK
E-mail: davide.dipaola@nottingham.ac.uk; amalia.patanè@nottingham.ac.uk

M. Bomers, Dr. L. Cerutti, Dr. A. N. Baranov, Prof. T. Taliercio
IES l'institut d'électronique
Univ. Montpellier and CNRS UMR 5214
F-34000 Montpellier, France

Prof. M. Capizzi
Dipartimento di Fisica
Sapienza Università di Roma
Piazzale A. Moro 2, 00185 Roma, Italy

Dr. M. Kesaria, Prof. A. Krier
Physics Department
Lancaster University
Lancaster LA1 4YB, UK

 The ORCID identification number(s) for the author(s) of this article can be found under <https://doi.org/10.1002/adom.201700492>.

© 2017 The Authors. Published by WILEY-VCH Verlag GmbH & Co. KGaA, Weinheim. This is an open access article under the terms of the Creative Commons Attribution-NonCommercial-NoDerivs License, which permits use and distribution in any medium, provided the original work is properly cited, the use is non-commercial and no modifications or adaptations are made.

DOI: 10.1002/adom.201700492

within a thin ($\approx 0.1\text{--}1\ \mu\text{m}$) channel below the surface.^[26] Secondary ion mass spectroscopy has shown that the H-distribution has a box-shaped form, from which the H-penetration depth can be estimated.^[26,27] Also, the N–H complexes are stable under normal conditions and do not degrade with time.^[27] In stark contrast to what observed in other dilute nitride alloys, such as Ga(AsN), Ga(PN), and (InGa)(AsN),^[28,29] the H-dopants in In(AsN) do not neutralize the electronic activity of the N-atoms. Thus, the band gap energy of In(AsN) does not change upon H-incorporation.^[27]

Here, we demonstrate that the H-enhanced conductivity near the surface of In(AsN) creates a surface plasmon polariton (SPP) mode confined at the air–semiconductor interface, which we detect via attenuated total reflection (ATR) measurements. The modulation of the carrier density by removal of H is demonstrated by laser annealing and Raman spectroscopy: the phonon–plasmon coupled mode induced by H can be suppressed locally by a thermal annealing with a focused laser beam. These findings demonstrate a new approach to MIR-plasmonics via postgrowth H-implantation and laser writing of In(AsN).

2. Results and Discussion

2.1. Reflectance Spectroscopy of Surface Plasmon Polaritons

For these studies, we used hydrogenated In(AsN) epilayers with thickness $t = 0.3\ \mu\text{m}$ ($1\ \mu\text{m}$) and N-content $x = 1\%$ (1.1%) grown by molecular-beam-epitaxy (MBE) on a GaAs substrate. We also examined control samples based on Si-doped InAs epilayers grown by MBE on an InAs substrate ($t = 1.3, 2.1,$ and $2.7\ \mu\text{m}$). The reflectance spectra on the In(AsN):H epilayers were acquired in the Brewster (Figure 1a) and the ATR (Figure 1b) configuration. Figure 1c shows the reflectance spectrum acquired in the Brewster configuration with light incident at an angle $\theta_i = 60^\circ$ to the normal to the surface of the epilayer (Figure 1a). The spectrum (solid black curve) shows a dip due to a Brewster mode,^[19] which we model using a transfer matrix formalism. Here, we consider p-polarized light impinging from air on a sequence of an In(AsN):H layer, a nonhydrogenated In(AsN) layer, and a semi-infinite nominally undoped GaAs substrate (dashed black curve in Figure 1c). We assume dielectric functions in the high frequency limit for air ($\epsilon_1 = \epsilon_{1\infty} = 1$), In(AsN) ($\epsilon_2 = \epsilon_{2\infty} = 12$), and GaAs ($\epsilon_3 = \epsilon_{3\infty} = 10.89$). The phononic and plasmonic contributions to the dielectric function of an In(AsN):H layer of thickness $t_H = 0.1\ \mu\text{m}$ are modeled

as $\epsilon_2(\omega, g, \omega_p) = \epsilon_{2\infty} \left(\frac{\omega_{\text{LO}}^2 - \omega^2 - i\gamma\omega}{\omega_{\text{TO}}^2 - \omega^2 - i\gamma\omega} - \frac{\omega_p^2}{\omega^2 + ig\omega} \right)$,^[19] where $\omega_{\text{TO}} =$

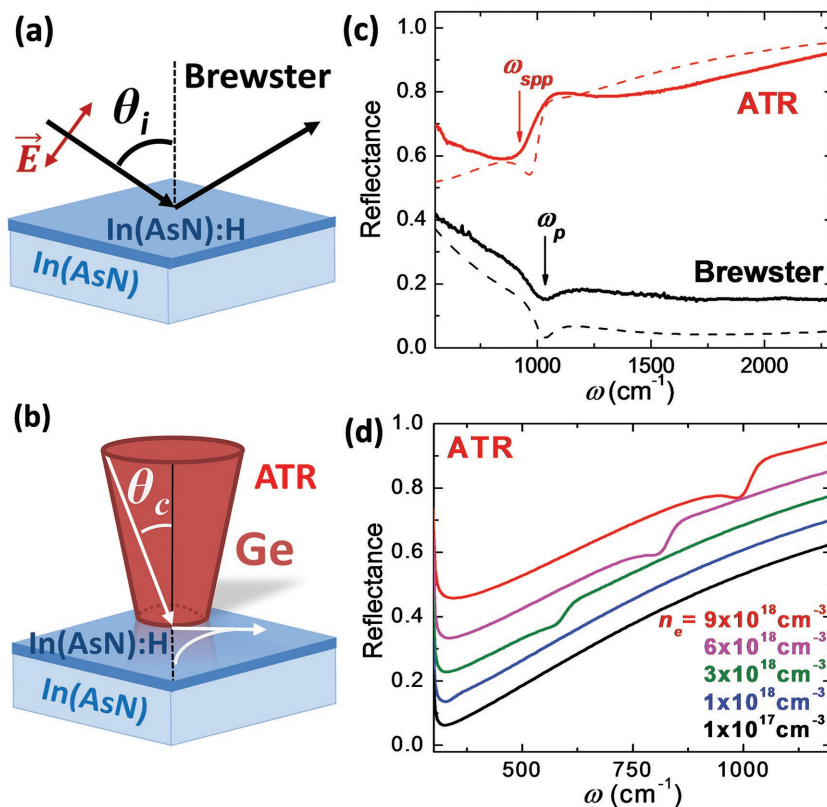


Figure 1. a) Sketch of reflectance in the Brewster configuration, with p-polarized light incident at an angle θ_i to the normal to the surface. b) Sketch of reflectance in the attenuated total reflection (ATR) configuration: light from a Ge prism undergoes total internal reflection at the interface with air at angles higher than the critical angle θ_c . c) Reflectance spectra for the In(AsN):H sample with thickness $t = 0.3\ \mu\text{m}$ in the Brewster (solid black line) and ATR (solid red line) configuration. The dashed curves represent the spectra as modeled with a transfer matrix formalism. d) Simulations of reflectance spectra in the ATR configuration for different carrier densities, n_e . For clarity, the spectra are shifted along the vertical axis relative to the curve at $n_e = 1 \times 10^{18}\ \text{cm}^{-3}$ (blue curve).

$218\ \text{cm}^{-1}$ and $\omega_{\text{LO}} = 239\ \text{cm}^{-1}$ are the frequencies of the transverse optical (TO) and longitudinal optical (LO) phonons, respectively, and $\gamma = 2.4\ \text{cm}^{-1}$ is the phonon broadening. The values of the plasma broadening, $g = 90\ \text{cm}^{-1}$, and the plasma frequency, $\omega_p = 985\ \text{cm}^{-1}$, are estimated from the fit to the data. Similar values are obtained for In(AsN):H epilayers with different thicknesses t (see Table 1). The values of ω_p correspond to electron densities $n_e = 8 \times 10^{18}\ \text{cm}^{-3}$ ($t = 0.3\ \mu\text{m}$) and $9 \times 10^{18}\ \text{cm}^{-3}$ ($t = 1\ \mu\text{m}$). The plasma frequency is given

Table 1. Plasma (ω_p) and surface plasmon polariton (ω_{spp}) frequencies in In(AsN):H epilayers.

| Sample | $\omega_p^{\text{a)}$ [cm^{-1}] | $\omega_p^{\text{b)}$ [cm^{-1}] | $\omega_{\text{spp}}^{\text{c)}$ [cm^{-1}] | $\omega_{\text{spp}}^{\text{d)}$ [cm^{-1}] |
|------------------------|---|---|--|--|
| $t = 0.3\ \mu\text{m}$ | 985 | 975 | 890–950 | 930 |
| $t = 1\ \mu\text{m}$ | 1050 | 1030 | 970–1000 | 990 |

^{a)}The value of ω_p is estimated by fitting the reflectance spectra in the Brewster configuration; ^{b)}the value of ω_p is estimated from the Raman shift of the L_{p}^+ mode; ^{c)} ω_{spp} is obtained from the ATR spectra; ^{d)} ω_{spp} is obtained from our calculations.

by $\omega_p = (n_e e^2 / m_e^* \epsilon_0 \epsilon_r)^{1/2}$, where e is the electron charge, m_e^* is the electron effective mass, ϵ_0 is the vacuum permittivity, and $\epsilon_r = 12$ is the relative permittivity. Nonparabolic effects on the first derivative electron mass, $m_e^* = \hbar^2 k / [d\epsilon(k)/dk]$, are accounted for by modeling the electron energy dispersion as $\epsilon(k)[1 + \alpha\epsilon(k)] = \hbar^2 k^2 / 2m_0^*$, where $\alpha = 2 \text{ eV}^{-1}$, $m_0^* = 0.025m_0$ at $k = 0$, and m_0 is the electron mass in vacuum.^[30] The difference in the values of n_e in the two epilayers is attributed to the 10% difference in the N-content in the two samples. These electron densities are also significantly larger than those in as-grown In(AsN) ($n_e \approx 10^{17} \text{ cm}^{-3}$).^[31,32]

As shown in Figure 1b, in the ATR configuration light impinges on the sample through a Ge prism at angles of incidence θ_i to the normal to the In(AsN) surface. In our experiment, θ_i ranges from 9.8° to 23.6° . Due to a thin air gap between the Ge prism and the sample surface (i.e., Otto configuration),^[33] light undergoes total internal reflection at the interface of Ge (refractive index $n_{\text{Ge}} = 4$) with air ($n_{\text{air}} = 1$) for angles θ_i higher than the critical angle $\theta_c = \sin^{-1}(n_{\text{air}}/n_{\text{Ge}}) \approx 14.5^\circ$, thus generating evanescent waves. In turn, these excite a SPP mode, which is confined to the surface and gives rise to a dip at frequency $\omega_{\text{spp}} \approx 900 \text{ cm}^{-1}$ in the reflectance spectrum (solid red curve in Figure 1c). In Figure 1d, we show simulations of the reflectance spectra in the ATR configuration for different carrier densities, n_e . The frequency ω_{spp} of the measured SPP mode is reproduced by the simulations for $n_e = 9 \times 10^{18} \text{ cm}^{-3}$. Decreasing n_e causes a redshift and weakening of the SPP mode. In particular, for carrier densities comparable to those observed in as-grown In(AsN) ($n_e \approx 10^{17} \text{ cm}^{-3}$),^[31,32] the reflectance spectrum shows no resonance, as also observed experimentally.

The ATR spectra were acquired at different positions, separated by $100 \mu\text{m}$ or 1 mm (see the insets in Figure 2a,b, respectively). In Figure 2a,b, we plot the signal as $\text{ATR} = -\log(I_R/I_I)$, where I_R and I_I are the intensities of the reflected and incident light beam, respectively. We observe that the frequency of the SPP resonance peak is nonhomogeneous over length scales of $\approx 1 \text{ mm}$ (Figure 2b). This variation is likely to be caused by the inhomogeneity of the as-grown material^[34] (see also Section S1 in the Supporting Information). The nonhomogeneous N-content and defects in In(AsN) may induce a nonuniform hydrogen incorporation. However, we note that the hydrogenation process is uniform: the standard deviation of the H-beam Gaussian profile ($\approx 2.5 \text{ cm}$) is much larger than the sample size ($\approx 0.4 \text{ cm}$). Plasmonic devices can be still developed on length scales where these variations are small ($< 100 \mu\text{m}$, Figure 2a). We measure values of ω_{spp} ranging from 890 to 950 cm^{-1} ($970\text{--}1000 \text{ cm}^{-1}$) for $t = 0.3 \mu\text{m}$ ($t = 1 \mu\text{m}$). These are smaller than ω_p and match well with those obtained by modeling the SPP dispersion for a single interface between air ($\epsilon_1 = 1$) and the In(AsN):H epilayer ($\epsilon_2(\omega) = \epsilon_{2\infty} - \omega_p^2 / (\omega^2 + i g \omega)$), see dashed red curve in Figure 1c and Table 1.

The dispersion of the SPP mode is given by $\omega = c k_{\parallel} \sqrt{(\epsilon_1 + \epsilon_2) / \epsilon_1 \epsilon_2}$, where c is the speed of light in vacuum and k_{\parallel} is the component of the wavevector parallel to the interface.^[33] Figure 2c shows the dispersion calculated for $g = 0$ (dashed black curve) and $g = 90 \text{ cm}^{-1}$ (solid black curve). For $g = 0$, the SPP dispersion approaches the surface plasmon frequency (green dot in Figure 2c) for infinite values of k_{\parallel} , i.e.,

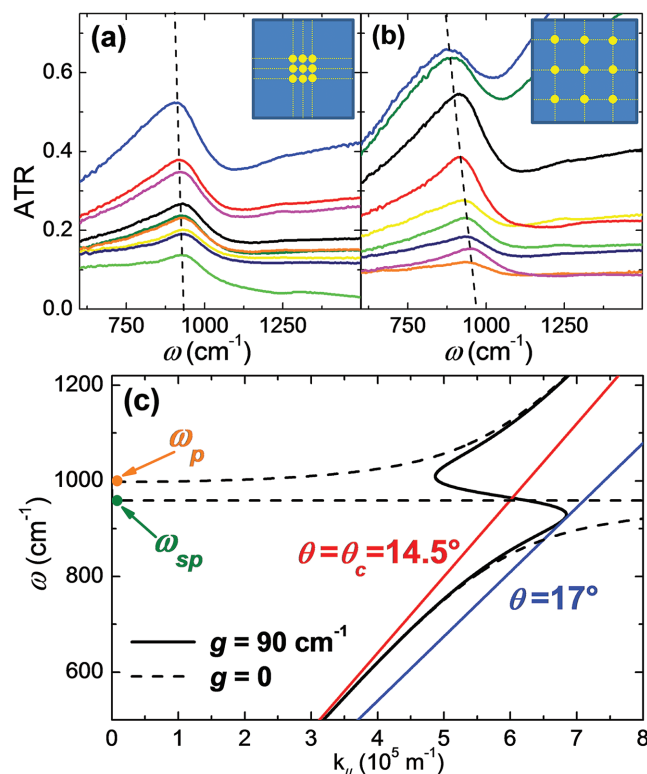


Figure 2. ATR spectra at positions separated by a) 0.1 mm and b) 1 mm for the In(AsN):H sample with thickness $t = 0.3 \mu\text{m}$. c) Dispersion for the SPP mode with broadening $g = 0$ (dashed black curve) and $g = 90 \text{ cm}^{-1}$ (solid black curve). The straight lines represent dispersions of the light cones from the Ge prism at $\theta = \theta_c = 14.5^\circ$ (red line) and $\theta = 17^\circ$ (blue line). The plasma (orange dot) and surface plasmon (green dot) frequencies are also shown at $k_{\parallel} = 0$.

$\omega_{\text{sp}} = \omega_p \sqrt{\epsilon_{2\infty} / (\epsilon_1 + \epsilon_{2\infty})} < \omega_p$ (orange dot in Figure 2c). For a finite broadening $g = 90 \text{ cm}^{-1}$, the SPP dispersion broadens and approaches ω_{sp} at finite k_{\parallel} . As indicated in Figure 2c, the SPP resonance can be excited if light from the Ge prism is incident at angles $14.5^\circ < \theta < 17^\circ$, consistent with the requirement for total internal reflection.

An air gap between the Ge prism and the In(AsN):H layer is required to achieve total internal reflection and thus observe the SPP mode. This can occur due to the natural tilting of the sample or can be induced intentionally. Figure 3a shows a color map of the integral of the reflectance intensity in the spectral range of the SPP mode. This reveals an intensity gradient, thus suggesting a natural tilting of the surface and the existence of an air gap between the Ge prism and the In(AsN):H epilayer. The blue areas in the color map correspond to regions with a larger air gap, thus leading to total internal reflection and the SPP resonance (Figure 3b). We estimate a small tilting of the surface at an angle $\phi^* \approx 0.5^\circ$. This corresponds to an air gap t_{air} of up to $\approx 0.9 \mu\text{m}$,^[35] consistent with the value obtained from the simulation of the ATR spectrum in Figure 1c ($t_{\text{air}} = 1 \mu\text{m}$, dashed red curve).

To probe further the role of this air gap, the ATR spectra were acquired for different tilted angles $\phi = 0^\circ\text{--}3^\circ$ of the In(AsN):H epilayer relative to the horizontal support of the

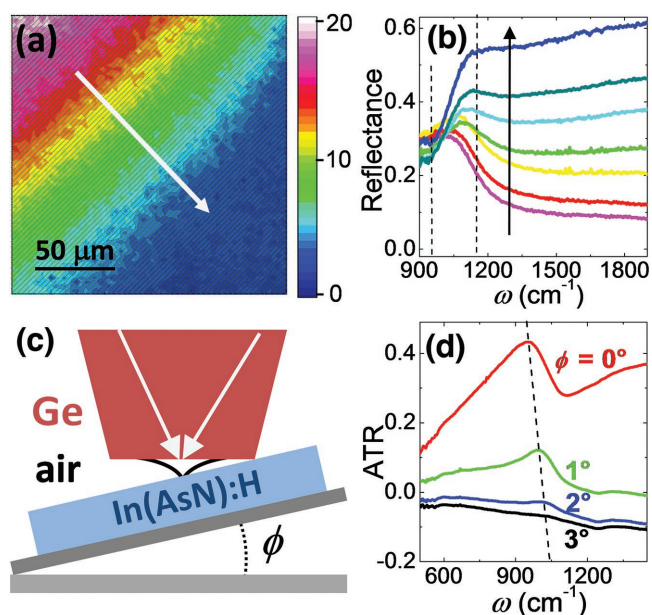


Figure 3. a) Integrated intensity of the reflectance signal from 950 to 1150 cm^{-1} for the In(AsN):H sample with thickness $t = 1 \mu\text{m}$. b) Reflectance spectra in the ATR configuration acquired along the arrow in the color map. c) Sketch of the modified ATR setup: the sample is tilted by an angle ϕ relative to the horizontal support. This creates an air gap between the Ge prism and the In(AsN):H epilayer. d) ATR spectra at various angles $\phi = 0^\circ\text{--}3^\circ$.

sample (Figure 3c,d): the SPP resonance tends to weaken and to blueshift with increasing ϕ . We attribute this behavior to the increase of the air gap with ϕ , thus leading to the exponential decay of the evanescent wave and a modified SPP $\omega\text{--}k_{\parallel}$ dispersion. A similar behavior is observed in highly doped InAs epilayers. Figure 4 shows the ATR spectra for an InAs sample with $t = 1.3 \mu\text{m}$ at tilted angles $\phi = 0^\circ\text{--}3^\circ$ (see also Section S2 in the Supporting Information).

2.2. Raman Spectroscopy of Plasma Modes

Further insights into the plasmonic effects were inferred from Raman spectroscopy studies. These were performed in the backscattering configuration with incident light of

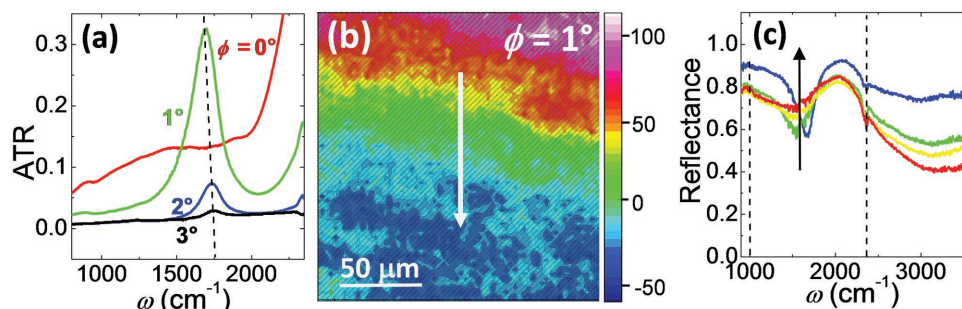


Figure 4. a) ATR spectra at angles $\phi = 0^\circ\text{--}3^\circ$ relative to the horizontal support of the samples for an InAs epilayer with thickness $t = 1.3 \mu\text{m}$. b) Intensity map of the reflectance signal integrated from 1000 to 2350 cm^{-1} . c) Reflectance spectra in the ATR configuration acquired along the arrow in the color map.

wavelength $\lambda = 633 \text{ nm}$. In Figure 5a, left panel, the comparison of the Raman spectrum of In(AsN) (blue curve) with that of In(AsN):H (red curve) evidences a broad feature $L_s^-(\omega_s^- = 231 \text{ cm}^{-1})$ between the TO ($\omega_{\text{TO}} = 218 \text{ cm}^{-1}$) and LO phonon frequency ($\omega_{\text{LO}} = 239 \text{ cm}^{-1}$). This feature weakens upon H-incorporation. The same comparison also shows the insurgence of a phonon–plasmon coupled mode, L_b^+ , centered at 975 cm^{-1} , in the Raman spectrum of In(AsN):H (red curve in Figure 5a, right panel).^[25,27]

The frequencies of the phonon–plasmon coupled modes L_b^\pm for bulk In(AsN):H and in the limit of wavevector $k \approx 0$ are given by^[36]

$$\omega_b^\pm = \frac{1}{\sqrt{2}} \sqrt{(\omega_p^2 + \omega_{\text{LO}}^2) \pm \sqrt{(\omega_p^2 + \omega_{\text{LO}}^2)^2 - 4\omega_p^2\omega_{\text{TO}}^2}} \quad (1)$$

The position of the L_b^+ mode, which has a strong dependence on n_e , corresponds to a plasma frequency consistent with that estimated from the reflectance spectra in the Brewster configuration (see Table 1). The Raman shift of the corresponding L_b^- mode is expected to coincide with that of the TO mode ($\omega_b^- = 218 \text{ cm}^{-1}$).

As regards the L_s^- mode, it is well known that a 2D surface accumulation layer forms in InAs^[37,38] and In(AsN).^[31] For a layer extending over a typical length l_s , the range of allowed wavevectors is $\Delta k \sim 2/l_s$, which can be comparable with the Thomas–Fermi screening wavevector. In this case, the surface LO-plasmon coupled mode, L_s^- , can be at a frequency intermediate between ω_{TO} and ω_{LO} .^[39–41] From the calculated dispersion, we estimate that the measured position of the L_s^- mode corresponds to a surface accumulation layer with thickness $l_s \approx 2 \text{ nm}$ (see Section S3 in the Supporting Information).

In summary, the Raman spectra reveal the “surface” L_s^- mode at $\omega_s^- = 232 \text{ cm}^{-1}$, the “bulk” L_b^- mode at $\omega_b^- = 218 \text{ cm}^{-1}$, and the L_b^+ mode at $\omega_b^+ = 975 \text{ cm}^{-1}$.

2.3. Tuning Plasma Modes by Laser Annealing

To study the tunability of plasmonic effects, the In(AsN):H samples were photoannealed with a focused laser beam with $\lambda = 633 \text{ nm}$ (Figure 5b). The light diffraction limit at this wavelength is given by the laser spot diameter $d = 1.22\lambda/\text{NA} \approx 1 \mu\text{m}$, where $\text{NA} (= 0.8)$ is the numerical aperture of our

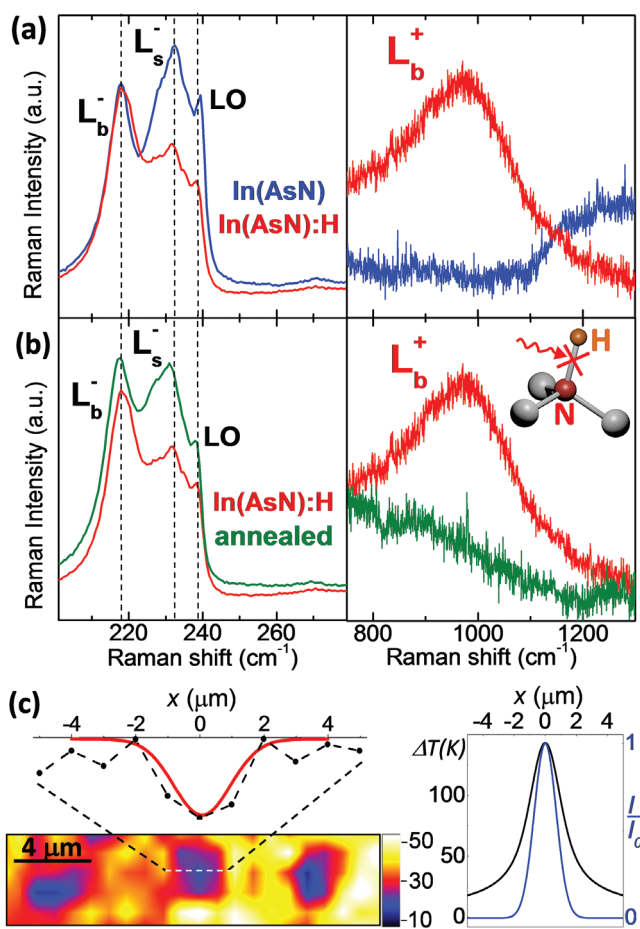


Figure 5. a) Raman spectra showing the L_b^- , L_s^- , LO (left panel), and L_b^+ (right panel) modes in In(AsN) (blue curve) and In(AsN):H (red curve). b) Raman spectra showing the L_b^- , L_s^- , LO (left panel), and L_b^+ (right panel) modes in In(AsN):H before (red curve) and after (green curve) laser annealing. Inset: sketch of the dissociation of the N–H bond due to laser excitation. c) Left: map of the L_b^+ intensity after laser annealing of three different spots, and profile of the L_b^+ intensity along the dashed line: dots connected by dashed lines are the data, the continuous red curve is the Gaussian fit to the data. Right: temperature increase, ΔT (black line) and normalized intensity of the laser beam, I/I_0 (blue line) versus position x .

100 \times objective. The annealing was performed at impinging powers up to $P = 15$ mW and exposure times $\tau \geq 300$ s. As shown in Figure 5b, following the laser annealing the intensity of the L_s^- mode is almost fully restored to that of the In(AsN) sample (left panel) and the L_b^+ feature disappears (right panel). This suggests the dissociation of the N–H bond and local removal of hydrogen from the lattice (see Inset of Figure 5b, right panel), thus restoring locally the pristine conditions of as-grown In(AsN).

Figure 5c (bottom left panel) shows the Raman map of the L_b^+ intensity over three different positions of the sample that are laser annealed. Three clear minima in the intensity are seen, thus confirming a local quenching of the L_b^+ mode. We fit the intensity distribution of the L_b^+ mode over the annealed spots with a Gaussian of full-width-half-maximum of ≈ 2 μm (top left panel), which is larger than the light diffraction limit

(≈ 1 μm). This broadening is attributed to a thermal effect:^[42] we estimate that the laser beam causes a temperature rise of up to $\Delta T = 140$ K that extends over a sample region wider than the laser spot (Figure 5c, right panel).^[43] We note that the annealing conditions used in our experiment do not cause any visible damage to the surface. In particular, atomic force microscopy studies of the surface of In(AsN):H before and after the laser annealing (Section S4, Supporting Information) indicate that for the range of laser powers (P up to 15 mW) and exposure times (τ up to 15 min) required to quench the L_b^+ mode, the laser annealing does not cause any topographic modification of the surface. Therefore, hydrogen-implantation followed by laser writing is a reproducible and nondestructive process that paves the way to patterning on a micrometric scale the In(AsN) plasmonic modes via a modulation of the material carrier density.

3. Conclusions

In summary, we demonstrated that the incorporation of hydrogen in the dilute nitride alloy In(AsN) with N-content of 1% induces a SPP mode at frequencies $\omega_{\text{spp}} \approx 900\text{--}1000$ cm^{-1} , which correspond to MIR wavelengths $\lambda \approx 10\text{--}11$ μm . We attribute the occurrence of this mode to the H-enhanced electron density. The N-atoms play a key role in the incorporation of hydrogen: they trap the H-atoms, whose small size and high diffusivity in the host crystal enables an increase in the electron density up to $n_e \approx 10^{19}$ cm^{-3} near to the surface. A similar increase of carrier density could be achieved for different N-concentrations under appropriate hydrogenation conditions.^[27] We demonstrated that plasmonic effects in In(AsN):H can be selectively suppressed on a micrometer scale by a local laser annealing. The dissociation of the N–H bond by laser writing offers a viable route to large-scale device fabrication and a means to pattern the electron density and plasmonic properties with micrometric resolution. The possibility to monitor the lateral size of the patterns, as well as the doping of the host crystal, could enable microscopic studies of plasmonic gratings and plasmonic phenomena near a surface, with potential for applications including detection of target gas fingerprints and molecular sensing in the MIR range. Compared to the traditional doping of InAs during the growth, which requires wet chemical etching to realize plasmonic gratings, the postgrowth H-doping of In(AsN) has potential for engineering plasmonic properties via the selective hydrogen incorporation and/or removal by laser writing.

4. Experimental Section

The nominally undoped dilute nitride In(AsN) epilayers were grown using a VG-V80H solid-source MBE reactor with a Veeco UNI-bulb radio frequency (RF) plasma nitrogen-source. In and Ga fluxes were provided by Knudsen thermal-effusion cells. The In(AsN) epilayers were grown at 450 $^\circ\text{C}$ using an RF power of 200 W and a nitrogen background pressure of 5×10^{-6} mbar. The layers were grown on 250 nm thick GaAs buffers on semi-insulating (1 0 0)-oriented GaAs substrates. In situ characterization was performed by reflection high energy electron diffraction. The as-grown In(AsN) epilayers were then hydrogenated using a Kaufman source under impinging H-dose $D_H = 3 \times 10^{17}$ ions cm^{-2} at the

temperature $T_H = 375$ °C for 2 h. Under these conditions, the hydrogen penetrates to a depth of about ≈ 0.1 μm below the surface.^[26]

The reflectance spectra in the Brewster configuration were acquired using a Hyperion 3000 microscope coupled to a Vertex 70 FTIR spectrometer with a Global light source, a polarizer, a KBr beam splitter, and a deuterated triglycine sulfate (DTGS) detector. The absorption coefficient $\alpha < 10^5$ m^{-1} at $\lambda = 2\text{--}10$ μm ^[44] gives an absorption length $l > 10$ μm . In the ATR configuration, a 20 \times ATR objective was used to focus the light beam through a Ge prism to a diameter $d \approx 100$ μm . The absorption length in this case is significantly smaller than in the Brewster configuration.^[33] The SPPs were excited in the Otto geometry, with a thin air gap between the Ge prism and the sample surface (Figure 3c). The air gap can appear due to a natural misorientation of the substrate or by using a controlled wedge. The light was detected using a mercury cadmium telluride detector. The ATR maps were obtained by using a focal planar array, with a spatial resolution of 2.5 μm at a wavelength $\lambda = 2.5$ μm , and by integrating the reflectance intensity variation with respect to a baseline. Raman spectroscopy studies were performed using a He–Ne laser ($\lambda = 633$ nm), an XY linear positioning stage, a LabRAM optical confocal microscope system, and a spectrometer with 1200 grooves mm^{-1} gratings, equipped with a Si charge-coupled device; the laser beam was focused to a diameter $d \approx 1$ μm using a 100 \times objective. An absorption length $l \approx 0.1$ μm at $\lambda = 633$ nm was estimated.^[45] The Raman spectra were measured at room temperature ($T = 300$ K) at a power $P < 1$ mW. The same experimental setup was used for local laser annealing experiments with powers up to $P = 15$ mW.

Supporting Information

Supporting Information is available from the Wiley Online Library or from the author. The data on which this manuscript is based are available as an online resource with digital object identifier (DOI) 10.17639/nott.324.

Acknowledgements

This work was supported by the Engineering and Physical Sciences Research Council [grant numbers EP/J015849/1, EP/J015296/1]; the EU Marie Skłodowska-Curie ITN-PROMIS [grant number 641899]; the French “Investment for the Future” Program [grant number EquipEx EXTRA, ANR 11-EQPX-0016]; the French ANR [grant number SUPREME-B, ANR-14-CE26-0015]; and the Occitanie region.

Conflict of Interest

The authors declare no conflict of interest.

Keywords

hydrogenation, mid-infrared, plasmonics, polaritons, semiconductors

Received: May 26, 2017

Revised: November 13, 2017

Published online: December 28, 2017

- [1] G. V. Naik, V. M. Shalaev, A. Boltasseva, *Adv. Mater.* **2013**, *25*, 3264.
 [2] P. R. West, S. Ishii, G. V. Naik, N. K. Emani, V. M. Shalaev, A. Boltasseva, *Laser Photonics Rev.* **2010**, *4*, 795.
 [3] F. Scotognella, G. Della Valle, A. R. Srimath Kandada, M. Zavelani-Rossi, S. Longhi, G. Lanzani, F. Tassone, *Eur. Phys. J. B* **2013**, *86*, 154.

- [4] M. Henini, M. Razeghi, *Handbook of Infrared Detection Technologies*, Elsevier, Oxford, UK **2002**.
 [5] Z. Han, P. Lin, V. Singh, L. Kimerling, J. Hu, K. Richardson, A. Agarwal, D. T. H. Tan, *Appl. Phys. Lett.* **2016**, *108*, 141106.
 [6] M. J. Milla, F. Barho, F. González-Posada, L. Cerutti, M. Bomers, J.-B. Rodriguez, E. Tournié, T. Taliercio, *Nanotechnology* **2016**, *27*, 425201.
 [7] D. Li, C. Z. Ning, *Opt. Express* **2011**, *19*, 14594.
 [8] F. B. Barho, F. Gonzalez-Posada, M. J. Milla, M. Bomers, L. Cerutti, T. Taliercio, *Opt. Express* **2016**, *24*, 16175.
 [9] E. F. Schubert, *Doping in III–V Semiconductors*, Cambridge University Press, Cambridge, UK **1993**.
 [10] S. B. Zhang, *J. Phys.: Condens. Matter* **2002**, *14*, R881.
 [11] C. M. Wolfe, G. E. Stillman, *Appl. Phys. Lett.* **1975**, *27*, 564.
 [12] D. M. Luz, S. S. Makler, E. V. Anda, *J. Phys. C: Solid State Phys.* **1988**, *21*, 5149.
 [13] A. Boltasseva, H. A. Atwater, *Science* **2011**, *331*, 290.
 [14] G. V. Naik, A. Boltasseva, *Phys. Status Solidi RRL* **2010**, *4*, 295.
 [15] G. V. Naik, A. Boltasseva, *Metamaterials* **2011**, *5*, 1.
 [16] E. Sacht, C. T. Shelton, J. S. Harris, B. E. Gaddy, D. L. Irving, S. Curtarolo, B. F. Donovan, P. E. Hopkins, P. A. Sharma, A. L. Sharma, J. Ihlefeld, S. Franzen, J.-P. Maria, *Nat. Mater.* **2015**, *14*, 414.
 [17] J. A. Schuller, R. Zia, T. Taubner, M. L. Brongersma, *Phys. Rev. Lett.* **2007**, *99*, 107401.
 [18] A. J. Hoffman, L. Alekseyev, S. S. Howard, K. J. Franz, D. Wasserman, V. A. Podolskiy, E. E. Narimanov, D. L. Sivco, C. Gmachl, *Nat. Mater.* **2007**, *6*, 946.
 [19] T. Taliercio, V. N. Guilengui, L. Cerutti, E. Tournié, J.-J. Greffet, *Opt. Express* **2014**, *22*, 24294.
 [20] Y. Zhong, S. D. Malagari, T. Hamilton, D. Wasserman, *J. Nanophotonics* **2015**, *9*, 093791.
 [21] E. Tokumitsu, *Jpn. J. Appl. Phys.* **1990**, *29*, L698.
 [22] S. Law, D. C. Adams, A. M. Taylor, D. Wasserman, *Opt. Express* **2012**, *20*, 12155.
 [23] T. D. Veal, L. F. J. Piper, P. H. Jefferson, I. Mahboob, C. F. McConville, M. Merrick, T. J. C. Hosea, B. N. Murdin, M. Hopkinson, *Appl. Phys. Lett.* **2005**, *87*, 182114.
 [24] R. Kudrawiec, J. Misiewicz, Q. Zhuang, A. M. R. Godenir, A. Krier, *Appl. Phys. Lett.* **2009**, *94*, 151902.
 [25] N. V. Kozlova, G. Pettinari, O. Makarovskiy, N. Mori, A. Polimeni, M. Capizzi, Q. D. Zhuang, A. Krier, A. Patanè, *Phys. Rev. B* **2013**, *87*, 165207.
 [26] A. V. Velichko, A. Patanè, M. Capizzi, I. C. Sandall, D. Giubertoni, O. Makarovskiy, A. Polimeni, A. Krier, Q. Zhuang, C. H. Tan, *Appl. Phys. Lett.* **2015**, *106*, 022111.
 [27] S. Birindelli, M. Kesaria, D. Giubertoni, G. Pettinari, A. V. Velichko, Q. D. Zhuang, A. Krier, A. Patanè, A. Polimeni, M. Capizzi, *Semicond. Sci. Technol.* **2015**, *30*, 105030.
 [28] R. Trotta, A. Polimeni, M. Capizzi, *Adv. Funct. Mater.* **2012**, *22*, 1782.
 [29] G. Ciatto, *Hydrogenated Dilute Nitride Semiconductors – Theory, Properties and Applications*, Pan Stanford Publishing, Singapore **2015**.
 [30] *Basic Semiconductor Physics* (Ed: C. Hamaguchi), Springer-Verlag, London **2006**.
 [31] A. Patanè, W. H. M. Feu, O. Makarovskiy, O. Drachenko, L. Eaves, A. Krier, Q. D. Zhuang, M. Helm, M. Goiran, G. Hill, *Phys. Rev. B* **2009**, *80*, 115207.
 [32] O. Drachenko, A. Patanè, N. V. Kozlova, Q. D. Zhuang, A. Krier, L. Eaves, M. Helm, *Appl. Phys. Lett.* **2011**, *98*, 162109.
 [33] S. A. Maier, *Plasmonics: Fundamentals and Applications*, Springer, New York, USA **2007**.
 [34] J. Ibáñez, R. Oliva, M. De la Mare, M. Schmidbauer, S. Hernández, P. Pellegrino, D. J. Scurr, R. Cuscó, L. Artús, M. Shafi, R. H. Mari,

- M. Henini, Q. Zhuang, A. Godenir, A. Krier, *J. Appl. Phys.* **2010**, *108*, 103504.
- [35] We estimate the natural tilting of the epilayer by performing the ATR studies for different tilted angles of the sample relative to the horizontal support, i.e., $\phi = 0^\circ$, $\pm 1^\circ$, etc. Since in both the $\phi = 0^\circ$ and $\phi = -1^\circ$ configurations, the ATR spectra are the same, by taking into account that the Ge prism has a cylindrical symmetry, we deduce that the natural tilting of the epilayer is $\phi^* \approx 0.5^\circ$. From the diameter of the contact zone of the Ge prism, $d_{Ge} = 100 \mu\text{m}$, we thus estimate an air gap of up to $\approx 0.9 \mu\text{m}$.
- [36] E. D. Palik, J. K. Furdyna, *Rep. Prog. Phys.* **1970**, *33*, 1193.
- [37] C. A. Mead, W. Q. Spitzer, *Phys. Rev. Lett.* **1963**, *10*, 471.
- [38] P. D. C. King, T. D. Veal, C. F. McConville, J. Zúñiga-Pérez, V. Muñoz-Sanjosé, M. Hopkinson, E. D. L. Rienks, M. F. Jensen, P. Hofmann, *Phys. Rev. Lett.* **2010**, *104*, 256803.
- [39] R. A. Cowley, G. Dolling, *Phys. Rev. Lett.* **1965**, *14*, 549.
- [40] S. Buchner, E. Burstein, *Phys. Rev. Lett.* **1974**, *33*, 908.
- [41] Y. B. Li, I. T. Ferguson, R. A. Stradling, R. Zallen, *Semicond. Sci. Technol.* **1992**, *7*, 1149.
- [42] M. Lax, *J. Appl. Phys.* **1977**, *48*, 3919.
- [43] This large increase of T is reached at relatively low powers due to the high absorption coefficient ($\alpha \approx 10^7 \text{ m}^{-1}$ at $\lambda = 633 \text{ nm}$) and low thermal conductivity ($K = 27 \text{ W m}^{-1} \text{ K}^{-1}$ at $T = 300 \text{ K}$) of In(AsN).
- [44] J. R. Dixon, J. M. Ellis, *Phys. Rev.* **1961**, *123*, 1560.
- [45] D. E. Aspnes, A. A. Studna, *Phys. Rev. B* **1983**, *27*, 985.